# An experimental investigation of local thermo-fluidic heat transfer in a U-shaped mini-channel sink

Giorgio Moscato[1,*], Giovanni P. Romano[1]

1: Dept. of Mechanical and Aerospace Engineering, University of Rome La Sapienza, Italy
* Correspondent author: giorgio.moscato@uniroma1.it

**Keywords**: PIV processing, Micro PIV, Microfluidics, Heat transfer

ABSTRACT

This study investigates experimentally a heated U-shaped mini-channel heat sink using Infrared Thermography and Particle Image Velocimetry for a water coolant flow of Reynolds numbers of 280, 650, and 1350 (based on the hydraulic channel diameter). The choice of this cell geometry is based on its role as a simplified unit of a serpentine heat exchanger, which is proved to be one of the most promising for cooling processes. The use of the infrared camera allows the detection of temperature fields on top of the external surface of the cell. Therefore, aiming to derive the temperature distribution on the channel roof, a dedicated transfer function is implemented. Moreover, we employed the lumped capacitance model for thermal analysis on both infrared measurements and thermocouple data. The latter are recorded to capture the cooling process of the aluminium base and water temperature at the end of the outlet tube. As a result, thermal transient rate, cooling magnitude and equilibrium temperature are obtained. These parameters indicate that higher Reynolds numbers correspond to increased thermal transient rates, enhanced cooling effects, and lower equilibrium temperatures. A non-uniform distribution of heat transfer along the channel is reported, with the most efficient cooling area localised close to the first 90-degree corner. These findings are consistent with numerical simulations and previous experimental observations. PIV results reveal the presence of two fluid acceleration zones following both 90-degree corners, which contribute to improve the water cooling ability in their respective regions. Additionally, the formation of two recirculating bubbles is reported at the inner wall from corners vertices, whose intensity is dependent on Reynolds number, pushing the main flow towards the outer channel wall and reducing the local heat transfer. Turbulent kinetic energy distributions are also investigated, pointing out the presence of intense areas that better match with regions of minimum equilibrium temperature than maximum velocity zones. This suggests the presence of local turbulent unsteadiness and three-dimensional phenomena, which contributes significantly to cooling enhancement.

## 1. Introduction

The study of microfluidic devices has gained a lot of attention in the last few decades, driven by the industrial interest in products such as electronic microchips, lab-on-chips and energy conversion systems. One of the crucial aspects related to those devices is their ability in exchanging

heat with an external fluid to control their temperature. This process is becoming increasingly demanding due to the rising trend of compacting powerful devices that require intensive cooling to maintain their performance. An everyday example is represented by smartphones or laptops. Even though considerable effort has already been dedicated to this aspect, most of the experimental works are focused on global heat transfer performance of such devices owing to the difficulties in obtaining reliable measurements at the micrometric scale. Nonetheless, the recent rise of new experimental methods for the measurement of local thermo-fluidic properties allows for a deeper understanding of this phenomenon. A comprehensive review of such techniques is reported by Morini (2019). Some attempts were performed by Sharma & Khan (2023) who studied numerically the differences in thermo-hydraulic behaviour between elliptic and sinusoidal-wavy serpentines for a laminar water flow at Reynolds numbers between 160-900. They kept the amplitude of microchannels fixed, while varying their wavelengths, and found that the elliptic-wavy serpentine showed better performances than the sinusoidal one in all conditions, except for the highest waviness at the lowest Reynolds number. Moreover, the authors performed an experimental validation of their results by means of a micro-PIV system, but only for the elliptical-wavy shape, at Re=160. Meanwhile, validation of the sinusoidal-wavy data was based on Sui et al. (2011) results. The latter investigated the overall Nusselt number and friction factor for copper wavy microchannels with a rectangular cross section of about 205×404 $\mu$m and amplitude varying from 0 to 259 $\mu$m. They measured temperature in the test section using 3 thermocouples, while two additional ones were located at the inlet and outlet, along with the connections of a differential pressure transducer. Furthermore, they compared their results to those obtained by straight channels with the same cross section and length, at Reynolds numbers between 300 to 800, along with three-dimensional conjugate simulations. The wavy shape outperformed the straight one in terms of heat transfer, though showing a larger pressure drop in the entire test range. This aspect represents a key point for microfluidic devices. Indeed, following Promvonge (2008), Kumar and colleagues (2019) and Spizzichino et al. (2020), thermal exchange efficiency can be expressed as the ratio between the mean Nusselt number and the friction factor (the latter raised to the power of 1 or 1/3). This formulation emphasizes the importance of incorporating fluid dynamic aspects into the optimization process of microfluidic devices, that should not focus solely on enhancing heat transfer capability. Dai and co-workers (2015) investigated five wavy (zigzag and sinusoidal shapes) microchannels separately, along with a straight one, of semi-circular cross-sections with diameter equal to 2 mm. They derived velocity fields through the use of a micro-PIV system, and temperature measurements thanks to miniature thermocouples. One of their main outcomes is the relevance of secondary flow structures (namely, Dean vortices) induced by the presence of bends, which enhance the heat transfer rates. Other authors pointed out similar considerations, both

numerically and experimentally, highlighting the occurrence of chaotic advection in wavy channels owing to a change in centrifugal force direction and the generation of Dean instability (Sui et al. 2011, Liu et al. 2023). However, in most of the experimental works, temperature is measured in a pointwise fashion due to the use of thermocouples which do not provide a full representation of the entire thermal field in channels without using numerical simulations (Abed et al. 2015, Khoshvaght-Aliabadi et al. 2016, Karale et al. 2013, Rastan H. et al. 2020). Infrared thermography (IRT) can be an answer to this problem. Following this idea, Metha and Khandekar (2012) investigated the thermal behaviour of a fully developed water laminar flow inside a mini-channel of square cross-section in a Reynolds number range of 100-850. They derived the local wall temperature distribution along the channel, in a direction parallel to the heat flux, with which they managed to estimate local heat transfer coefficient and thus local axial Nusselt number. The latter showed high values in the early thermal development region, with a decreasing trend in streamwise direction for all Reynolds numbers. Moreover, they performed numerical simulations that underlined the presence of conjugate heat transfer and two heat flux variation scenarios. In the first one, owing to a high conductivity ratio (i.e. the ratio between the solid and fluid conductivities) and low Reynolds numbers, a constant temperature could be assumed at the solid-fluid interface. Meanwhile, for high Reynolds numbers and low conductivity ratio, an almost constant heat flux condition was achieved.

However, as mentioned earlier, the study of fluid motion is of primary relevance in the optimization process of mini/microfluidic devices. In order to investigate this aspect, a promising approach involves the use of a microPIV system (Morini G.L. 2019, Sharma et al. 2023, Wereley & Meinhart 2007). Recently, Wang et al. (2023) successfully adopted a combined approach of PIV and IRT to investigate the enhancement in heat transfer in a U-shaped square channel of hydraulic diameter equal to 45.5mm with detached curved ribs.

The present work aims to study a U-shaped mini water-cooled heat sink from both thermal and fluid dynamic points of view. To achieve this goal, IRT and micro high-speed PIV systems are implemented. The U-shaped channel has been selected as a simplified unit of the serpentine heat exchanger, which is considered one of the most promising for cooling processes (Spizzichino et al. 2020). We investigate three Reynolds numbers (about 280, 650 and 1350, based on the hydraulic diameter) and a wall temperature of 50 °C. Velocity and thermal fields are detailed to derive insights into heat transfer enhancement resulting from fluid motion.

## 2. Experimental set-up

A sketch of the experimental apparatus is reported in Figure 1. The hydraulic system is composed of a syringe pump Landgraff LA-800 (absolute error ±0.05 ml/min) that pushes the piston of a 140 ml plastic syringe (placed inside an aluminium case to avoid any expansion during compression) full of demineralised water at ambient temperature (about 21.5 °C), a heated test cell and a discharge bowl. In order to prevent heat losses after the exit of the cell, a plastic outlet tube coated with a thermal insulation layer in neoprene is placed between the cell and the discharge bowl. Our U-bend channel has a square cross-section of hydraulic diameter equal to 2 mm and emulates the one numerically investigated by Liou et al. (2018). It is milled in a Plexiglass plate of 100 mm in length, 15 mm in width and 4 mm in thickness. Other geometrical data along with a picture of the assembled cell are reported in Figure 2. The top and side walls of the channel are made of Plexiglass and considered adiabatic, while the bottom side is closed by an aluminium basement of the same length of the Plexiglass cell and cross-section of 10x15 mm. In order to avoid leakages at high flow rates, a soft aluminium sealing is fabricated and placed between the plexiglass and the base. Its thickness is about 2 mm and it is black painted for seeding enhancement in PIV images. Six M3 screws and a M2 one are used to fix the cell to the base. They are coated with PTFE to minimize their thermal influence on the cell.

The heat source is represented by a Stuart US-150 hot plate, placed in direct contact with the aluminium basement. Its temperature is set to 50°C for all measurements.

Water temperature is measured in the syringe before the pumping phase using a thermometer XS Temp 7 NTC with a resolution of 0.1°C, and at the end of the outlet tube by means of a K-type thermocouple (diameter equal to 0.5 mm, resolution of 0.1°C and an accuracy of ±1°C). Moreover, another K-type thermocouple is placed inside the aluminium base, about 1 mm below the channel floor, in the middle of the U-bend, to monitor the temperature stability and the water cooling effect.

Temperature spatial fields in the test cell are obtained using an infrared camera Optris PI400i (288x381 px at 1 Hz, accuracy of ±2 °C, thermal sensitivity of 75 mK) placed on top of the cell. It is equipped with the Optris O53 wide angle lens, providing a field of view of approximately 11.33x15 mm at the object plane, with a spatial resolution of about 40 $\mu$m/px. A dedicated radial image distortion correction is directly applied in the IR camera software. The IR camera working distance used in this work is about 5 mm from the cell, which is outside the manufacturer's suggested design range. Therefore, to ensure reliable and consistent measurements between the IR camera and the thermocouples, several tests were conducted to investigate their correlation. Strictly speaking, the Plexiglass cell is directly heated with the hot plate and its external surface temperature is measured using both infrared thermography (IRT) and a thermocouple placed in direct contact with it. A PTFE cloak is also used to prevent convective heat transfer between the thermocouple's tip and the surrounding air. Then, thermocouple data are fitted with IR camera

ones, which are derived from the average of a 3x3 pixels window close to the thermocouple position. In this way, the IR measurements are calibrated to match the thermocouple readings. However, as previously reported, the IR camera measures the cell's external surface temperature. Therefore, aiming to derive the internal cell thermal field at the interface between Plexiglass and the coolant (i.e. at the channel roof), a transfer calibration function is implemented. Similarly to Mohamed (2023) approach, we performed IRT and thermocouple measurements at four hot plate temperatures, namely 30°C, 50°C, 70°C and 90°C. Unlike the previous IR camera calibration, this time the thermocouple is placed in a hole allowing it to touch the top surface of the channel. The latter is filled with water at rest. A linear regression is then applied to derive the mathematical function that enables to "transfer" the temperature data from the external cell surface to the roof of the channel.

Speaking about the microPIV system, it is composed of a 12-bit CMOS Photron AX100 Mini high-speed camera (sensor size of 20.48 x 20.48 mm) equipped with three Kenko extension tube (two 36 mm and one 12 mm, respectively) and a Nikkor 50mm f/1.2 lens. The resulting spatial resolution is 12 $\mu$m/px. Acquisitions are performed at 4000 fps (for the lowest flow rate), 6800 fps and 7200 fps (for the highest flow rate condition) with an exposure time of 0.125 ms, 0.1 ms and 0.08 ms respectively. Hollow spherical glass particles of mean diameter equal to 15 $\mu$m, standard deviation 10 $\mu$m and Stokes number about $10^{-5}$ are used as seeding. Meanwhile, two 40 W LED white lamps guarantee a volumetric illumination.

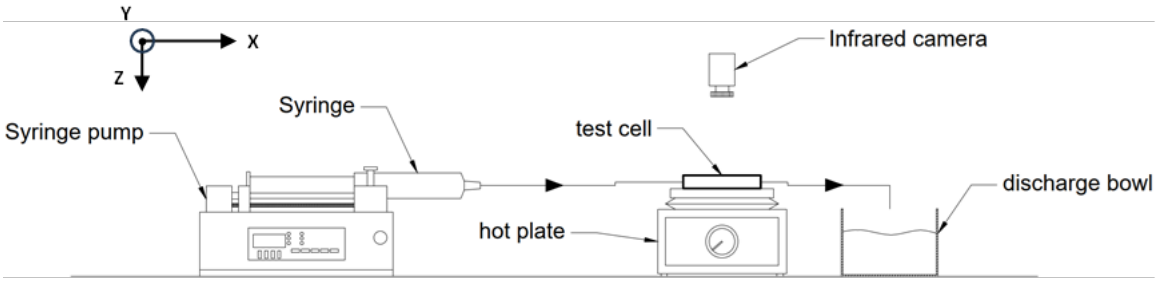


**Figure. 1** Sketch of the hydraulic system from syringe pump to discharge bowl. Infrared camera and high-speed camera (not reported here) are placed on top of the test cell. Infrared camera position is reported merely to illustrate the practical positioning of objects.

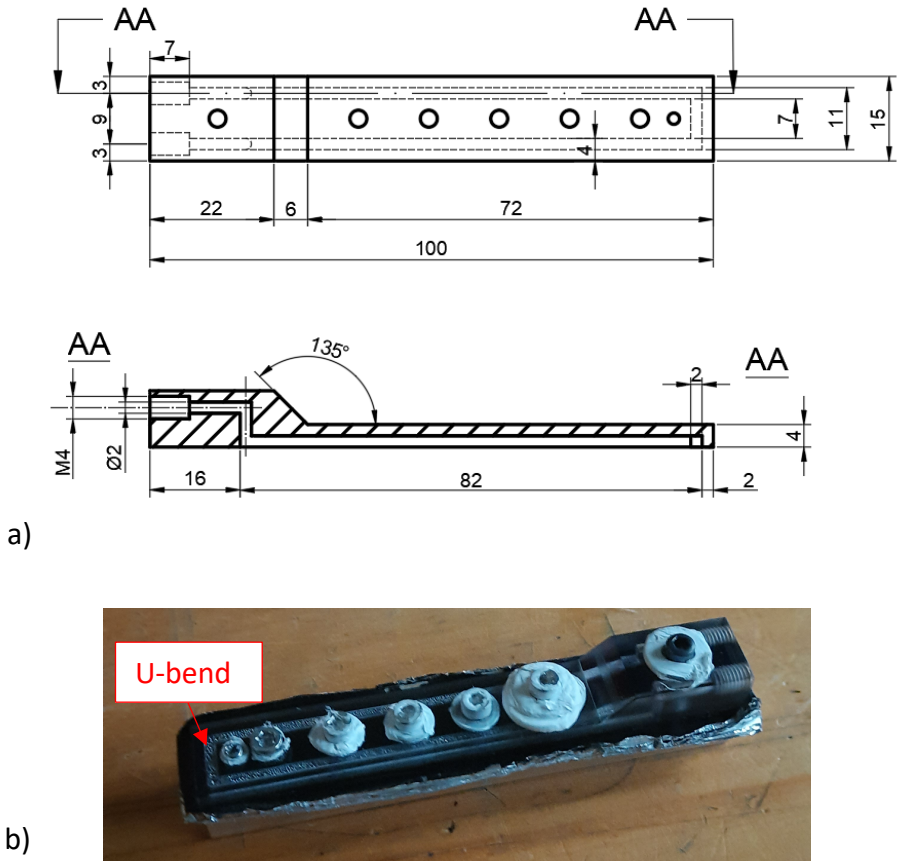


**Figure. 2** Sketch of the U-bend channel (a) and picture of the assembled cell (b). Dimensions in (a) are reported in mm.

A ten-partitions' recording scheme is also implemented to improve the quality of statistics (Moscato & Romano, 2023).

The investigated flow rates are 30 ml/min, 70 ml/min and 150 ml/min, corresponding to Reynolds numbers of approximately 280, 650, and 1350, respectively. These Reynolds numbers are based on the hydraulic diameter $D_h$ = 0.002 m and the kinematic viscosity calculated at the bulk water temperature, defined as the average between the water temperature at the outlet tube exit and the one in the syringe.

## 3. Results and discussion

### *3.1 IR camera calibration and thermal transfer function*

In order to obtain consistent temperature measurements between thermocouples and IR camera, their relationship is investigated. Hereby, we placed our Plexiglas cell in direct contact with the hot plate and record its temperature both with IR camera and thermocouple. Results are reported in Figure 3 for temperatures equal to about 30°C, 40°C, 50°C, 60°C and 70°C. They show a clear

linear trend, with differences of few degrees for each temperature. For instance, at 50°C, IR camera seems to slightly overestimate the temperature of about 2-3°C compared to thermocouple measurements. Nonetheless, keeping in mind the thermocouple accuracy of ±1°C and the IR camera one of ±2°C, these differences could find a reasonable justification. However, aiming to refer all thermal measurements on the thermocouples (which are considered more reliable), the linear calibration function is applied to correct IR data. In Table 1 we report the fitting coefficients, along with their 95% confidence intervals, root-mean-square-error and the R-square coefficient.

Furthermore, to derive thermal data on top of channels from external IR measurements, a thermal transfer function is needed. Similar to the IR calibration function, we collect measurements using both the IR camera and a thermocouple, the latter being placed in direct contact with the water in the upper part of the channel. The fluid is at rest. According to Mohamed (2023), the best correlation between the internal (channel) and external surface temperatures is represented by a linear regression. The author pointed out that these results are independent of the fluid's nature and the thermal process considered (i.e., heating or cooling conditions). Our findings support these claims, as the relationship between the IR camera and thermocouple data exhibits a clear linear trend (Figure 4). In Table 1, we show the regression coefficients, along with their 95% confidence intervals, root-mean-square-error and the R-square coefficient.

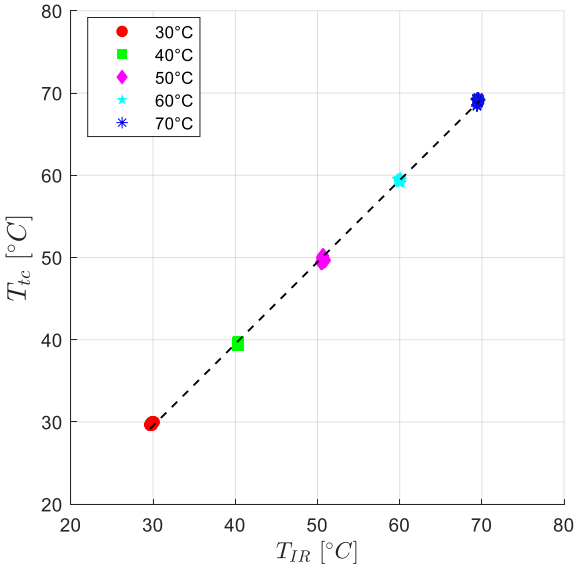


**Figure. 3** Scatter plot and linear fitting curve of thermocouple measurements (y-axis) and IR camera data (x-axis) for calibration function.

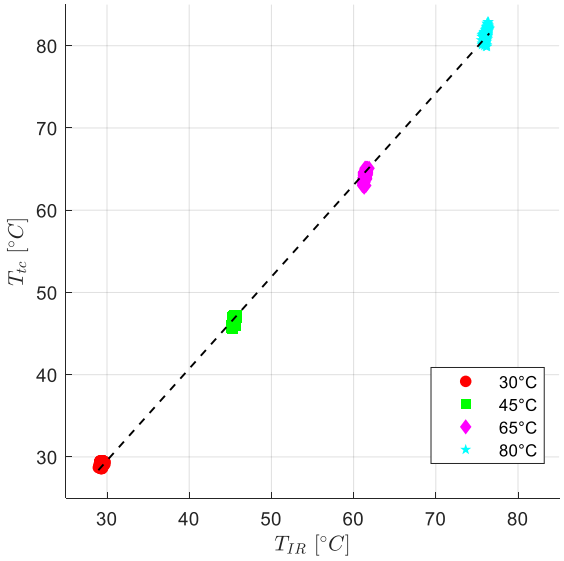


**Figure. 4** Scatter plot and linear fitting curve of thermocouple measurements (y-axis) and IR camera data (x-axis) for thermal transfer function.

**Table. 1** Linear fitting parameters for IR camera calibration function and transfer function are presented. The coefficients p1 and p2 represent the slope and intercept, respectively, of the linear equation in the form y = p1*x + p2. The 95% confidence bounds for these values are provided in parentheses.

| | **IR camera calibration func.** | **Thermal transfer func.** |
|---|---|---|
| **p1** | 0.995 (0.9919, 0.9981) | 1.117 (1.114, 1.119) |
| **p2** | -0.3035 (-0.4657, -0.1413) | -3.944 (-4.086, -3.802) |
| **R-square** | 0.9992 | 0.9992 |
| **RMSE** | 0.3848 | 0.5537 |

*3.1 Aluminium base and coolant results*

First of all, we determine the hydrodynamic and thermal state of the flow when approaching the U-bend zone of the cell. The distance between the latter and the channel's inlet is about 39 hydraulic diameters. Following the definitions reported by Cengel (2009), the hydrodynamic and the thermal entry lengths in laminar conditions are evaluated as follows:

$$x_{h,lam} \approx 0.05 Re D_h \,, \qquad (1)$$

$$x_{th,lam} \approx 0.05 Re Pr D_h \,, \qquad (2)$$

where $D_h$ is the hydraulic channel diameter, $Re$ is the Reynolds number based on $D_h$ and $Pr$ is the Prandtl number. All water properties are computed at the water bulk temperature. The latter is defined as the average between the water temperature measured in the syringe, and the stable one reached at the end of the outlet tube.

Our results show that measurements at Reynolds number equal to 280 and 650 fall into a hydrodynamically developed but thermally developing state. Meanwhile, for the highest flow rate, a simultaneous developing regime is reported (Table 2). These regimes are undoubtedly of practical interest due to the varying geometries and dimensions of mini-channel sinks. In particular, at high Reynolds numbers, it can be challenging to achieve a hydrodynamically fully developed flow because it requires a longer distance that could not be available in the device.

In Figure 5 we report the temporal temperature evolution derived by the thermocouple placed at the midpoint of the U-turn, in the channel floor, for all tests. To highlight the decay trends, temperature values are divided by the hot plate temperature $T_0$. At the beginning of the observation, the temperature is stable at the hot plate value and the syringe pump is off. Then, once the cooling water start to flow inside the cell, a decreasing trend is reported. In agreement with well-known literature findings (Cengel 2009, Incropera et al. 1996), the latter is characterized by an exponential decay:

$$T(t) = T_\infty + \Delta T_\infty e^{-\frac{t}{\tau}}, \qquad (3)$$

where $T_\infty$ is the stabilization temperature that is reached for an infinite time, $\Delta T_\infty$ is the difference between the initial temperature $T_0$ and $T_\infty$ (thus it represents the overall cooling magnitude) and $\tau$ is the thermal transient time constant. Nonetheless, owing to the finite syringe's volume, the duration of tests allows to reach clearly the equilibrium temperature only in the lowest Reynolds number case. Meanwhile, for the middle flow rate, the temperature is approaching its stable condition, and for the highest flow rate it is still in the thermal transient regime. However, the amount of acquired data is sufficient to perform the fitting described in equation 3. In this way, the equilibrium temperature, cooling effect and thermal transient rate are estimated for all measurements and presented in Table 3. Interestingly, the lowest flow rate case shows the highest $T_\infty$, the lowest cooling effect and the greatest time constant. As a general outcome, the equilibrium temperature and the time constant are inversely proportional to Reynolds numbers, while the cooling magnitude increases as the Reynolds number increases. Introducing the non-dimensional parameter $\theta_{wall}$, defined as:

$$\theta_{wall} = \frac{T(t) - T_\infty}{T_0 - T_\infty}, \qquad (4)$$

it is possible to focus solely on the exponential part of equation 3, and plot it logarithmically to obtain a linear trend (Figure 5), whose slope represents the transient rate (i.e., $1/\tau$). Even though differences are small, it is still possible to appreciate how the highest transient rate is associated to the highest Reynolds numbers, thus confirming the exponential fitting results of Table 3.

**Table. 2** Required hydrodynamic and thermal entry lengths for current measurements.

| | Re=280, Pr=6.2 | Re=650, Pr=6.4 | Re=1350, Pr=6.44 |
|---|---|---|---|
| $x_{h,lam}/D_h$ | 14.0 | 32.5 | 67.4 |
| $x_{,th,lam}/D_h$ | 86.5 | 208.2 | 434.0 |

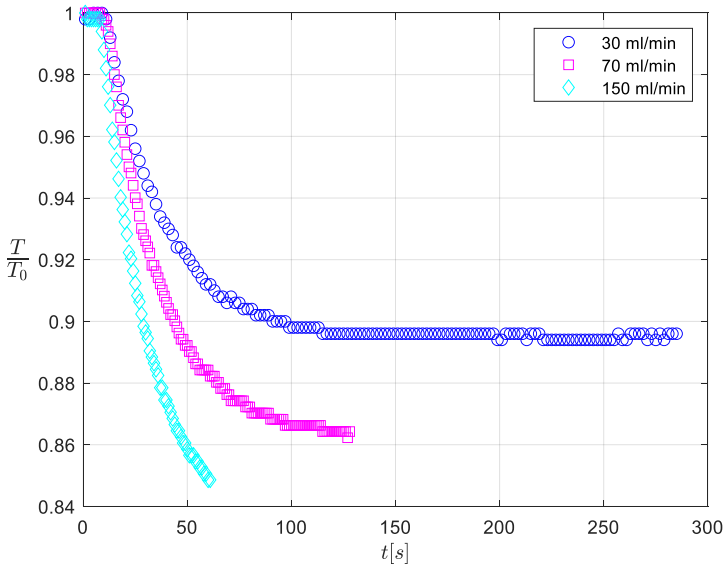


**Figure. 5** Non dimensional temperature profile in time obtained from a thermocouple placed in the aluminium base, at 0.5mm below the middle of the channel in the U-bend zone. $T_0$ is the hot plate temperature.

**Table. 3** Exponential fitting parameters described in equation 3 for base thermocouple measurements. $T_\infty$, $\Delta T_\infty$ and $\tau$ are provided with their 95% confidence bounds in parentheses.

| | Re=280, Pr=6.2 | Re=650, Pr=6.4 | Re=1350, Pr=6.44 |
|---|---|---|---|
| $T_\infty$ [°C] | 44.75 (44.75, 44.76) | 43.24 (43.22, 43.25) | 41.8 (41.75, 41.86) |
| $\Delta T_\infty$ [°C] | 5.375 (5.343, 5.407) | 6.844 (6.81, 6.878) | 8.533 (8.485, 8.58) |
| $\tau$ [s] | 27.17 (26.92, 27.43) | 25.04 (24.76, 25.32) | 22.44 (22.03, 22.85) |

In addition, we analyzed the water temperature derived at the end of the outlet tube. Similarly to $\theta_{wall}$, it is possible to define the corresponding parameter $\theta_{water}$ for the fluid. Non-dimensional temperature and $\theta_{water}$ temporal profiles are reported in Figure 7(a-b). Results show that the equilibrium temperature is achieved in each Reynolds number condition (Figure 7a). Notably, the highest Reynolds number flow reaches a stable condition in a faster way, and its final temperature is the lowest. This is further confirmed by Figure 7b, where a linear trend is still observable in all cases, before the temperature becomes stable. Herein, the highest slope (i.e. thermal transient rate) is associated to the highest Reynolds number.

According to Morini & Yang (2013), the average Nusselt number can be estimated as:

$$\overline{Nu} = \frac{D_h}{k}\frac{\dot{m}c_p\left(T_{b,out} - T_{b,in}\right)}{A_s(T_0 - T_b)}, \tag{5}$$

where $k$ is the thermal conductivity of the fluid, $\dot{m}$ is the flow rate, $A_s$ is the heat transfer surface, $T_{b,out}$ and $T_{b,in}$ are the bulk fluid temperature at the inlet and outlet sections respectively, and $T_b$ is the fluid bulk temperature defined as the arithmetic average of $T_{b,out}$ and $T_{b,in}$.

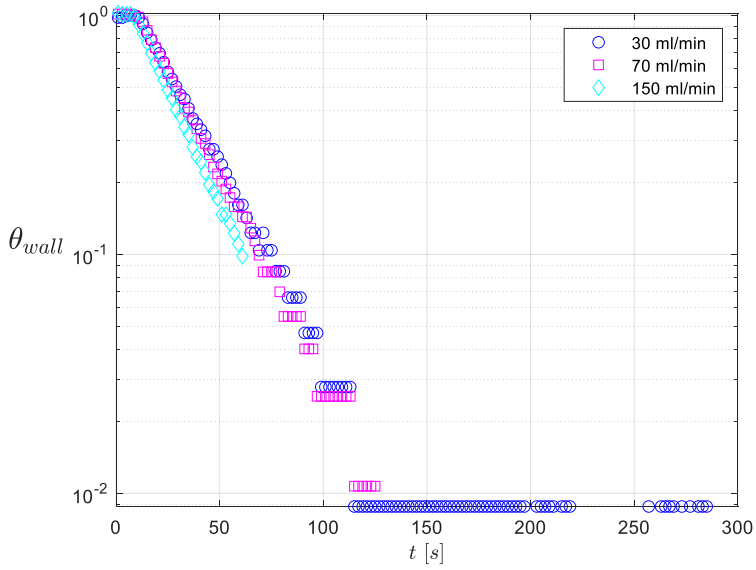


**Figure. 6** Normalised $\theta_{wall}$ temporal profile, obtained from a thermocouple placed in the aluminium base, at 0.5mm below the middle of the channel in the U-bend zone.

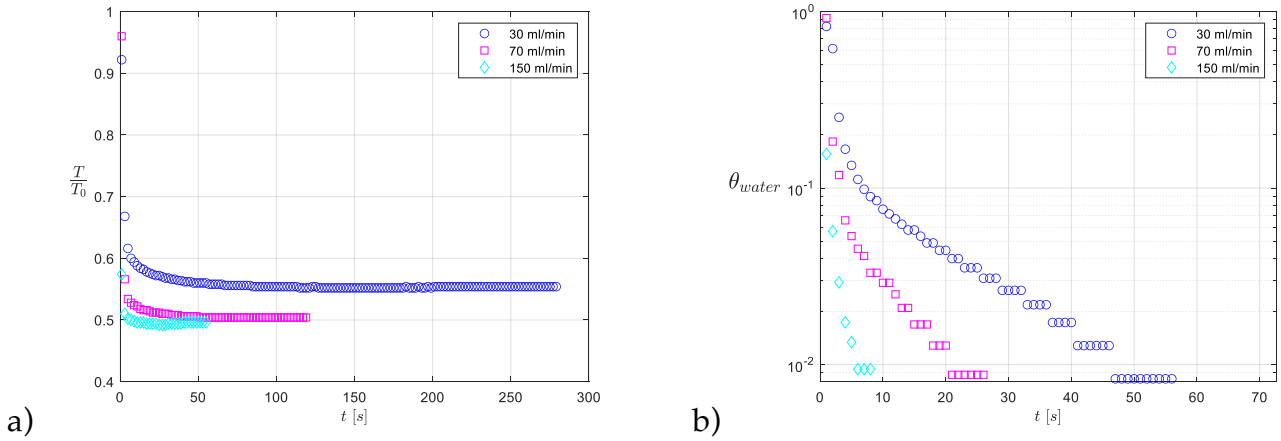


**Figure. 7** Non-dimensional temporal temperature profile (a), and normalised $\theta_{water}$ temporal profile (b), obtained from a thermocouple placed at the end of the outlet tube. $T_0$ is the hot plate temperature. In Figure (b), we focus only in the linear region of trends, thus the reported x and y-axis are limited accordingly.

Figure 8 shows our results along with experimental ones of Spizzichino et al. (2020) for a standard serpentine cell of $D_h$ equal to 1 mm, of Lee et al. (2004) for a rectangular microchannel of $D_h$ equal to 318 μm, and the well-known Sieder&Tate correlation (1936) evaluated in our conditions. The average Nusselt number increases with increasing Reynolds number, suggesting a growing dominance of the convection contribution over conduction. Values are quite in agreement with Spizzichino et al. (2020), while they match Lee et al. (2004) only at the highest Reynolds number case. Speaking about Sieder & Tate correlation, it does not overlap our results, even though differences are relatively small, and trends are similar. Even though the number of our points does not allow to derive a clear and reliable fitting, we can speculate that differences with Sieder&Tate correlation could be ascribed to the different conditions in which the correlation was derived (i.e. straight channel and simultaneous developing of hydraulic and thermal boundary layer).

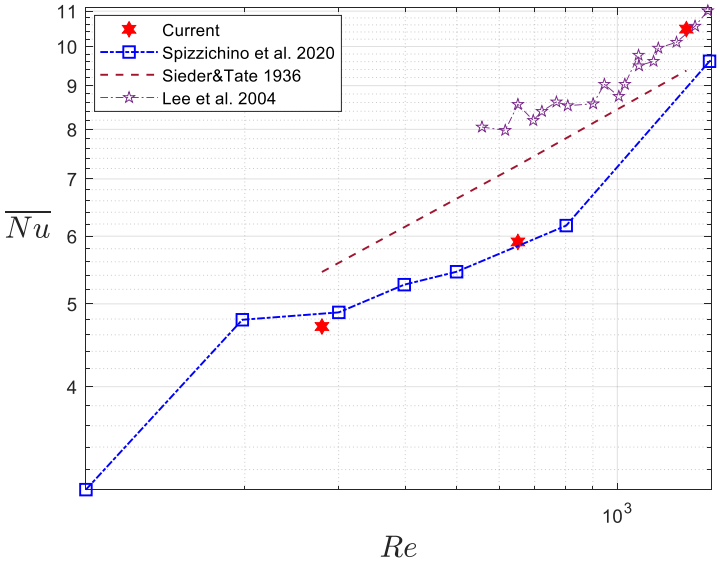


**Figure. 8** Average Nusselt number for different Reynolds numbers. Current experimental data are reported together with literature experimental results and Sieder & Tate correlation.

*3.2 Infrared thermography results*

In order to derive a spatial description of the U-bend channel's temperature field, we used an infrared camera pointing towards the external top surface of the cell. After calibrating the recorded images, the transfer function is applied, enabling us to derive the temperature spatial distribution along the channel's roof, inside the cell. Similarly to the no-slip flow condition of a fluid over a solid surface, in thermal processes a no-temperature-jump condition is defined at the contact point (Cengel, 2009). Consequently, the fluid layer adjacent to the solid wall has the same temperature as the surface itself, and the heat transfer occurs purely by conduction. Therefore, we can consider

the temperature distribution at the top of the channel as representative of that of the water in contact with it.

Following the same approach used in thermocouple data analysis, each pixel in IR images can be treated as a localized point source of temperature (a "lump") which follows the exponential temperature decay model of equation 3 (so-called "lumped capacitance model"). Strictly speaking, the validity of this model is typically assessed for a Biot number range below 0.1, where the internal conductivity is more effective than external convection, so that a spatial uniform temperature can be assumed. In our study, we cannot consider a uniform temperature distribution along the channel. Nevertheless, if we focus on a single-pixel region, its dimension is so small that the resulting Biot number is sufficiently low to make this assumption. Moreover, the IR camera records a single temperature value for each pixel, and with a sufficiently high spatial resolution, the resulting discretization allows us to capture the main spatial differences in temperature across a surface. In our case, we deal with a resolution of about 40 $\mu$m/px, with a channel cross-section of about 50 times the single-pixel unit. Therefore, we can accurately detect spatial temperature differences along the channel. As a result, we compute the three exponential fitting parameters of equation 3, namely $T_\infty$, $\Delta T_\infty$ and $\tau$ for each pixel.

Figure 9 shows the non-dimensional thermal transient rate $b=1/\tau$ (Figure 9a), cooling magnitude (Figure 9b) and equilibrium temperature's (Figure 9c) spatial distributions along the U-bend channel for Reynolds number equal to 280. The flow is coming from the bottom-left side (see the red arrow in Figure 9a). The thermal transient rate is made non-dimensional by multiplying it by the hydraulic diameter and dividing it by the thermal diffusivity of water at its syringe bulk temperature. Interestingly, all parameters exhibit a non-uniform distribution of their values along the channel, suggesting a different heat transfer ability depending on the location. For instance, thermal transient rate reveals its highest values in an area slightly after the first 90-degree turn, which is further displaced towards the outer wall of the channel. Then, its magnitude decreases, and at the end of the entire U-bend, it attains a lower intensity compared to the entrance. A similar spatial evolution is observed also for the cooling effect, with a corresponding lowest equilibrium temperature zone placed in the upper-left corner of the first pass. These findings agree with the numerical and experimental results of Liou et al. (2018) for Re=200 and aspect ratio equal to 1, and Wang et al. (2023) for Re=10000. Indeed, the authors pointed out the presence of a large high Nusselt number region in the middle of the channel, after the first 90-degree corner. This was ascribed to the downwash cooling effect of a secondary flow associated to two counter-rotating primary Dean vortices. Moreover, they observed the presence of two separation bubbles close to the inner wall. The first one was located after the corner vertex corresponding to $X/D_h \cong 2.2$ and $Y/D_h \cong 2.7$ in our Figure 9, meanwhile the second one was placed after the inner corner vertex of

the second 90-degree bend. Their presence can explain our thermal results in these regions, where the transient rate, cooling magnitude and equilibrium temperature indicate less efficient heat transfer.

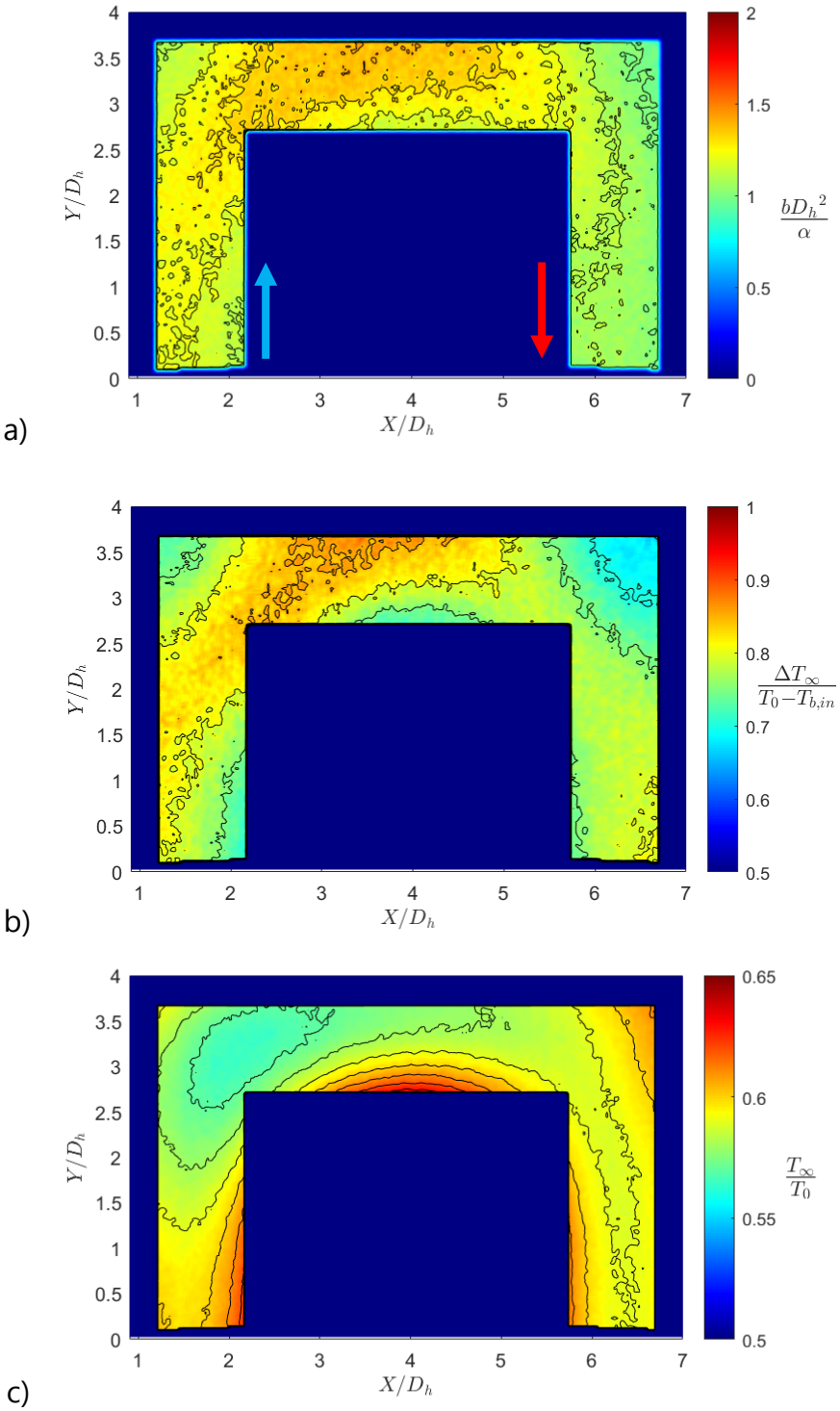


**Figure. 9** Spatial maps from IR thermography for Re=280 of non-dimensional thermal transient rate $b$ (a), cooling magnitude $\Delta T_\infty$ (b) and equilibrium temperature $T_\infty$ (c). The flow is coming from the bottom-left side of the U-bend cell, as shown by blue and red arrows in (a). Contour lines are reported each 0.1 (a), 0.05 (b) and 0.01 (c).

All outcomes derived for Reynolds number equal to 280 can be extended to Reynolds number 650 and 1350 (Figure 10). However, this time the thermal transient rate shows higher values than Re=280, that suggests a faster cooling and thus confirms our previous findings of thermocouple data analysis.

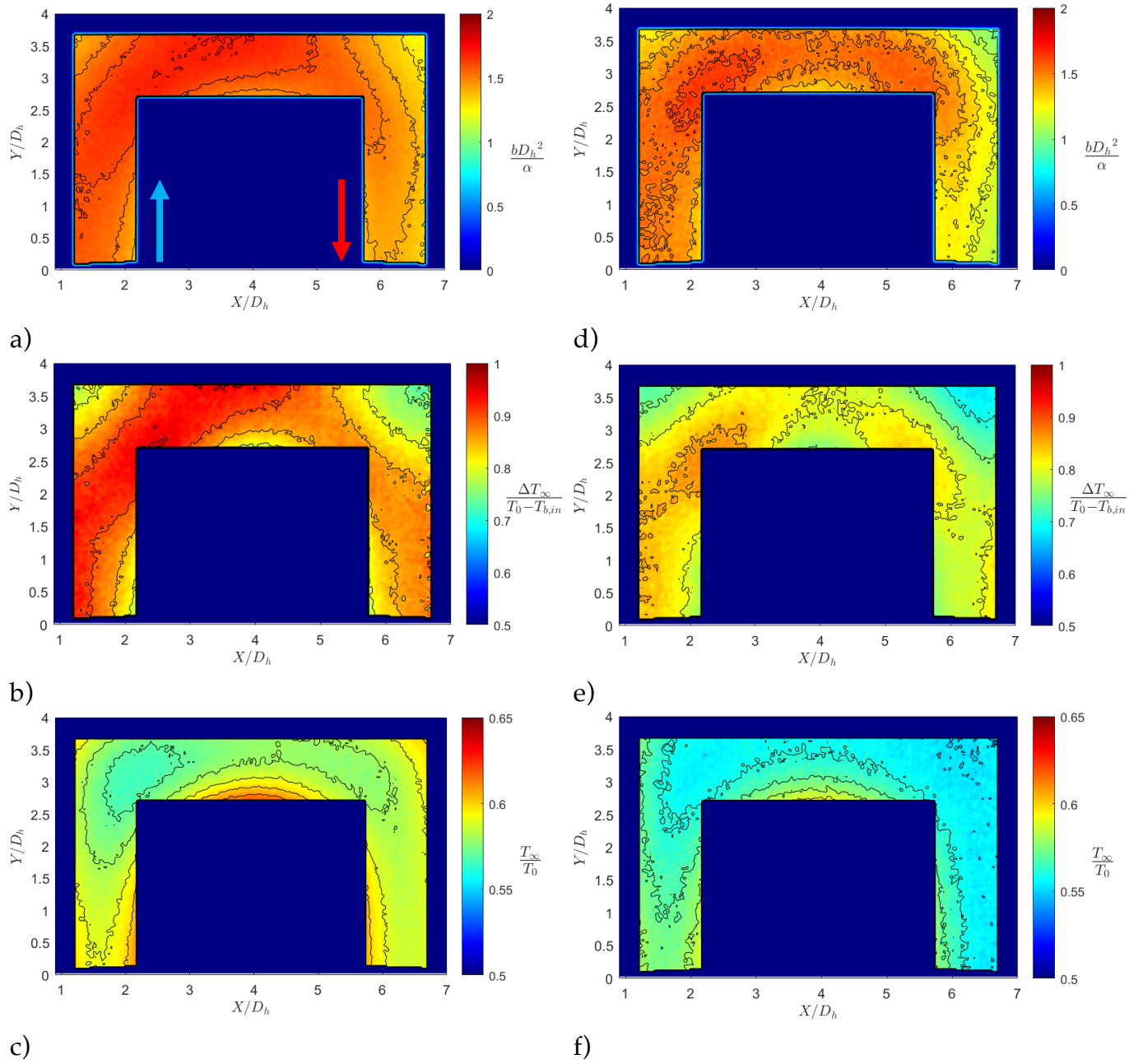


**Figure. 10** Spatial maps from IR thermography for Re=650 (a, b, c) and Re=1350 (d, e, f) of non-dimensional thermal transient rate b (a, d), cooling magnitude $\Delta T_\infty$ (b, e) and equilibrium temperature $T_\infty$ (c, f). The flow is coming from the bottom-left side of the U-bend cell, as shown by blue and red arrow in (a). Contour lines are reported each 0.1 (a, d), 0.05 (b, e) and 0.01 (c, f).

Interestingly, in the highest Reynolds number case, the area with the highest transient rate is more concentrated in the first corner, while a lower uniformity compared to Re=680 is observed in the second half of the U-turn. Moreover, the cooling magnitude point out smaller values in the fastest flow condition than that of the middle Reynolds number. This discrepancy may be attributed to a potential small difference in the initial temperature of Plexiglas and to a greater uncertainty in the fitting process for the highest Reynolds number. Indeed, in the latter case, owing to the finite volume of the syringe, acquisitions last about 60 seconds only, and this contribute to the rise of uncertainty when implemented the fitting model. For instance, in the midpoint of the entire U-channel, at $X/D_h \cong 3.95$ and $Y/D_h \cong 3.2$, we observe 95% confidence intervals of 1.45% (referred to the average parameter value) for the equilibrium temperature and 6.5% for the cooling magnitude. Meanwhile, at Re=650, the corresponding values in the same position are about 0.275% and 5.9%.

*3.3 Particle Image Velocimetry results*

In order to further detailed our previous thermal outcomes, the fluid motion is investigated by means of PIV. In Figure 11a-c, we report the non-dimensional average (in time) velocity magnitude for all Reynolds numbers, computed as:

$$\frac{\overline{U(x,y)}}{U_b} = \frac{\overline{\sqrt{u(x,y,t)^2 + v(x,y,t)^2}}}{U_b} \tag{6}$$

where $u$ and $v$ are the velocity components in X and Y direction, respectively, and $U_b$ is the bulk velocity derived from the flow rate. As reported by Liou et al. (2018) for Re=200, we can see two high velocity regions for all our Reynolds numbers, one at the end of the first 90-degree corner, and the other one near the outer wall, after the second corner of the U-bend. They both reach a peak of about two times the bulk velocity. Speaking about the first one, it matches quite well the elongated areas of high thermal transient rate of Figure 9 and Figure 10, thus confirming a strict relation between the main flow velocity and the cooling velocity. Meanwhile, the second one has a good correspondence with the high cooling magnitude effect and low equilibrium temperature distribution in the second pass of the cell. Herein, for Re=280, the velocity peak is not in direct contact with the outer wall, as reported by Liou et al. (2018). However, for higher flow rates, it is pushed even further towards the outer wall. This fact can be attributed to the effect of the centrifugal force (which is a velocity-dependent quantity), along with presence of a recirculating bubble located at the inner wall of the second 90-degree corner. The latter is highlighted by vorticity fields of Figure 11d-f, where a high vorticity region at the inner vertex of the second 90-degree corner is observed for all Reynolds numbers. A similar behaviour is also observed for

another recirculation bubble, placed at the inner vertex of the first U-bend corner, that correspond to the first velocity peak region.

However, if we compare the equilibrium temperature results of Figures 9-10 to the velocity fields of Figure 11, it is clear that the position of maximum velocity does not perfectly match the minimum temperature in all conditions, as one might have expected. Therefore, aiming to derive a more detailed understanding, turbulent kinetic energy is evaluated and reported in Figure 12.

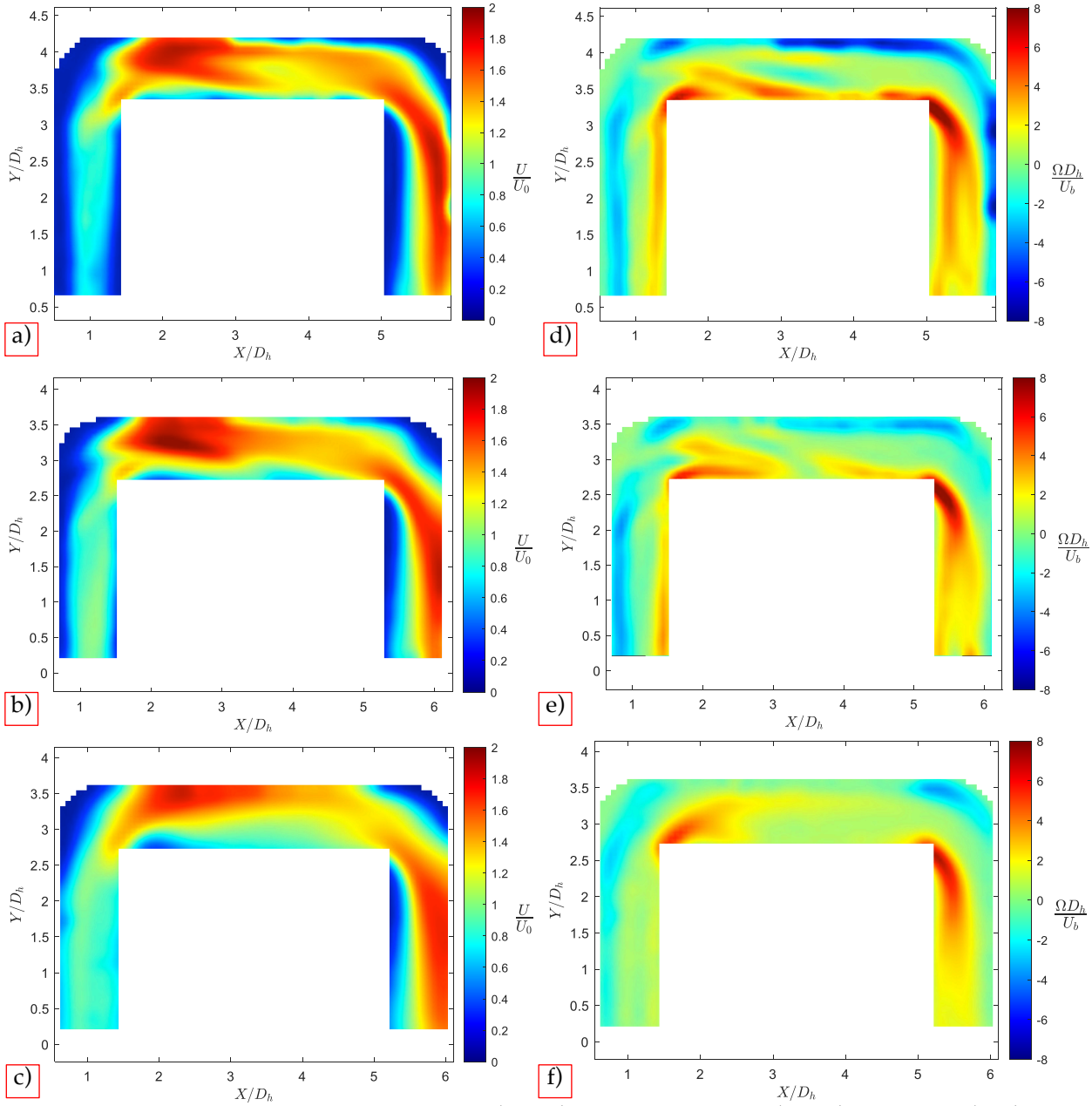


**Figure. 11** Non-dimensional average velocity fields (a, b, c) and vorticity fields (d, e, f) for Re=280 (a, d), Re=650 (b, e), and Re=1350 (c, f).

It is strictly related to both velocity components' fluctuations and can be used as an indicator of high unsteadiness and three-dimensional effects of secondary flow phenomena such as Dean

vortices. Notably, it reveals a distinct spot of high values in the first pass corner for all Reynolds numbers, whose peak always spatially precedes that of the velocity. Hence, this area of high turbulence can be responsible for the highest heat removal along the channel, thus leading to the lowest wall equilibrium temperature.

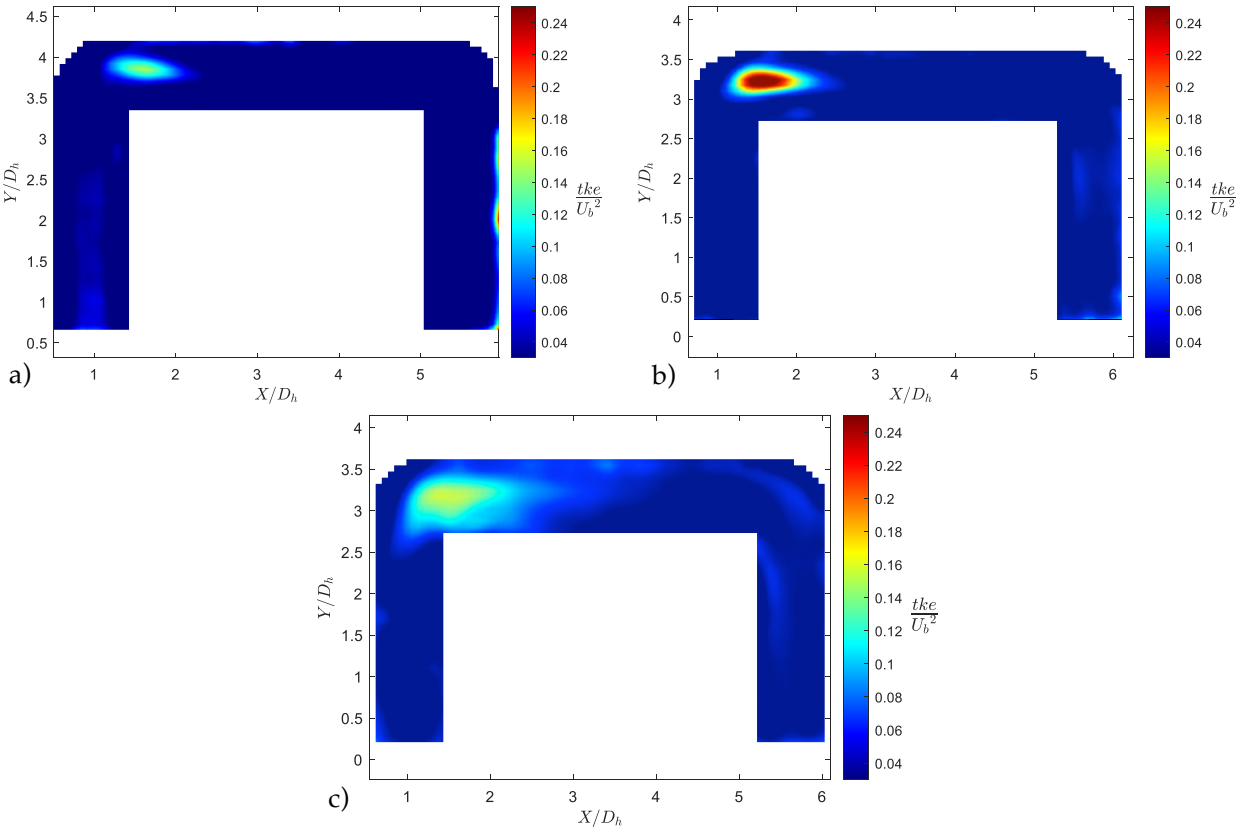


**Figure. 12** Non-dimensional turbulent kinetic energy for Re=280 (a), Re=650 (b), and Re=1350 (c).

## 4. Conclusions and remarks

In this work we investigated a heated U-shaped mini-channel heat sink from both thermal and fluid motion perspectives. Infrared Thermography and Particle Image Velocimetry were employed to obtain the spatial temperature distribution and velocity field of cooling water along the channel at three Reynolds numbers, i.e. 280, 650 and 1350. From a thermal point of view, the lumped capacitance model was successfully employed to evaluate the thermal transient rate and time, cooling effect and equilibrium temperature, based both on infrared measurements and thermocouple data. The following main remarks are drawn:

- Higher Reynolds number flows are characterised by higher thermal transient rates, cooling effects and lower equilibrium temperatures.

- There is a non-uniform distribution of the heat transfer along the channel, with the most efficient cooling area localised in the first pass, at the 90-degree corner, regardless of Reynolds number.
- Two fluid acceleration zones are detected, one following the first 90-degree corner, and the other after the second 90-degree turn. They partially account for the greater heat transfer localised in those regions.
- An area of intense turbulent kinetic energy, situated at the exit of the first 90-degree corner, preceding the point of maximum velocity, qualitatively matches with the region of minimum equilibrium temperature. This suggests the presence of a turbulence action and three-dimensional effects that contribute to a significant localised cooling enhancement.

## Acknowledgments

The authors would like to acknowledge Mohammad Moradi and Niccolò Iorio for their help during the experimental campaign. Special thanks also go to Jais Mohamed and Michela Spizzichino for their work on the device conceptualization, characterization and for the optimization of measurement techniques. Alessandro Caterina and Maximo Orlando Capponi are also thanked for their contributions to device manufacturing and suggestions for improving the experimental setup. The authors acknowledge the Financial support by PNRR - PE02 - NEST - Spoke 5.

## References

Abed, W. M., Whalley, R. D., Dennis, D. J., & Poole, R. J. (2015). Numerical and experimental investigation of heat transfer and fluid flow characteristics in a micro-scale serpentine channel. *International Journal of Heat and Mass Transfer, 88*, 790-802.

Cengel, Y. A. (2009). *Heat transfer: a practical approach*. MacGraw Hill, New York, 210.

Dai, Z., Fletcher, D. F., & Haynes, B. S. (2015). Impact of tortuous geometry on laminar flow heat transfer in microchannels. *International Journal of Heat and Mass Transfer, 83*, 382-398.

Incropera, F. P., DeWitt, D. P., Bergman, T. L., & Lavine, A. S. (1996). *Fundamentals of heat and mass transfer*. New York: Wiley.

Karale, C. M., Bhagwat, S. S., & Ranade, V. V. (2013). Flow and heat transfer in serpentine channels. *AIChE journal, 59(5)*, 1814-1827.

Khoshvaght-Aliabadi, M., Sahamiyan, M., Hesampour, M., & Sartipzadeh, O. (2016). Experimental study on cooling performance of sinusoidal–wavy minichannel heat sink. *Applied Thermal Engineering, 92*, 50-61.

Liou, T. M., Wang, C. S., & Wang, H. (2018). Nusselt number and friction factor correlations for laminar flow in parallelogram serpentine micro heat exchangers. *Applied Thermal Engineering*, *143*, 871-882.

Liu, X., Fu, Y., Wang, J., & Ge, J. (2023). Dean instability and thermal characteristic in sinusoidal structure. *International Journal of Heat and Mass Transfer*, *206*, 123938.

Mehta, B., & Khandekar, S. (2012). Infra-red thermography of laminar heat transfer during early thermal development inside a square mini-channel. *Experimental thermal and fluid science*, *42*, 219-229.

Mohamed J., *Global and Local Characterization of Small-Scale Heat Transfer Devices* (2023), PhD thesis, Sapienza University of Rome.

Morini, G. L. (2019). The challenge to measure single-phase convective heat transfer coefficients in microchannels. *Heat Transfer Engineering*, *40(9-10)*, 695-710.

Morini, G. L., & Yang, Y. (2013). Guidelines for the determination of single-phase forced convection coefficients in microchannels. *Journal of heat transfer*, *135*(10), 101004.

Moscato, G., & Romano, G. P. (2023). A comparative study of circular and rectangular bended plunging jets. *Experimental Thermal and Fluid Science*, *145*, 110888.

Promvonge, P. (2008). Thermal augmentation in circular tube with twisted tape and wire coil turbulators. *Energy Conversion and Management*, *49(11)*, 2949-2955.

Ranjith Kumar, V., Balasubramanian, K., Kiran Kumar, K., Tiwari, N., & Bhatia, K. (2019). Numerical investigation of fluid flow and heat transfer characteristics in novel circular wavy microchannel. *Proceedings of the Institution of Mechanical Engineers, Part E: Journal of Process Mechanical Engineering*, *233(5)*, 954-966.

Rastan, H., Abdi, A., Hamawandi, B., Ignatowicz, M., Meyer, J. P., & Palm, B. (2020). Heat transfer study of enhanced additively manufactured minichannel heat exchangers. *International Journal of Heat and Mass Transfer*, *161*, 120271.

Sharma, A., & Khan, M. K. (2023). Heat transfer and flow characteristics of varying curvature wavy microchannels. *International Journal of Thermal Sciences*, *185*, 108096.

Spizzichino, M., Sinibaldi, G., & Romano, G. P. (2020). Experimental investigation on fluid mechanics of micro-channel heat transfer devices. *Experimental Thermal and Fluid Science*, *118*, 110141.

Sui, Y., Lee, P. S., & Teo, C. J. (2011). An experimental study of flow friction and heat transfer in wavy microchannels with rectangular cross section. *International journal of thermal sciences*, *50(12*), 2473-2482.

Vasilev, M. P., Abiev, R. S., & Kumar, R. (2019). Effect of microchannel heat sink configuration on the thermal performance and pumping power. *International Journal of Heat and Mass Transfer*, *141*, 845-854.

Wang, C. S., Wang, E. S., Huang, Y. J., & Liou, T. M. (2023). PIV and IRT measurements of hydrothermal performance in a U-shaped heat exchanger with 3D printed detached curved ribs. *International Journal of Heat and Mass Transfer, 201*, 123562.

Wereley, S. T., & Meinhart, C. D. (2010). Recent advances in micro-particle image velocimetry. *Annual review of fluid mechanics, 42*, 557-576.